Supplementary Materials for

Supramolecular cocrystals built through redox-triggered ion intercalation in π-conjugated polymers

Yu Yamashita, Junto Tsurumi, Tadanori Kurosawa, Kan Ueji, Yukina Tsuneda, Shinya Kohno, Hideto Kempe, Shohei Kumagai, Toshihiro Okamoto, Jun Takeya, and Shun Watanabe

Correspondence and requests for materials should be addressed to swatanabe@edu.k.u-tokyo.ac.jp (S.W.)

Contents

1. Supplementary methods and discussion

1.1 Materials and doping methods

The polymeric semiconductor poly[2,5-bis(3-tetradecylthiophen-2-yl)thieno[3,2-*b*]thiophene] (PBTTT-C14), which is one of the most widely studied p-type semiconductors,[1,2] was purchased from Sigma-Aldrich and used as received. The molecular weight of PBTTT is estimated to be 40,000 to 80,000. *o*-dichlorobenzene (*o*DCB) as a solvent for PBTTT was purchased from the FUJIFILM Wako Pure Chemical Corporation (Wako). The acceptor dopant 2,3,5,6-tetrafluoro-7,7,8,8-tetracyano-quinodimethane (F4TCNQ) was purchased from Tokyo Chemical Industry (TCI), and molybdenum tris(1-(trifluoroacetyl)-2-(trifluoromethyl)ethane-1,2-dithiolene) (Mo(tfd-$COCF_3$)$_3$) was purchased from Sigma-Aldrich. For anion exchange doping, lithium bis(trifluoromethanesulfonyl)imide (Li-TFSI) was purchased from TCI and used as received. A series of salts composed of tris(4-bromophenyl)amine (TPA) radical cation, including tris(4-bromophenyl)ammoniumyl bis(trifluoromethylsulfonyl)imide (TPA-TFSI) and tris(4-bromophenyl)ammoniumyl hexafluorophosphate (TPA-PF_6), was synthesized and purified in-house (details of chemical synthesis appear elsewhere). Tris(4-bromophenyl)ammoniumyl hexachloridoantimonate (TPA-$SbCl_6$), known as "magic blue", was purchased from Sigma-Aldrich.

PBTTT thin films were fabricated on low-impurity EAGLE XG glass substrates, except for those used in the photoemission yield spectroscopy (PYS) analysis. The PYS data were obtained on indium-tin-oxide (ITO) substrates. PBTTT thin films were deposited via spin-coating from 1-wt% *o*DCB solutions with a spinning speed of 2,000 rpm for 1 min. The resulting films were annealed on a hotplate at 180 °C for 1 h, then slowly cooled to room temperature. The film thicknesses were determined to be 42 ± 2 nm using a Dektak surface profilometer and atomic force microscopy measurements.

The PBTTT thin films were doped by immersing solid-state thin films into dopant solutions for 10 min in N_2-purged vials. The concentration of dopants and employed solvents are listed in Supplementary Table S1. After cooling the vial to room temperature, the film was removed from the vial and the residual solvent was blown off under a flow of N_2.

Dopant	Solvent	Concentration	Process temperature
F4TCNQ	*n*-butyl acetate	5 mM	60 °C
F4TCNQ/Li-TFSI	*n*-butyl acetate	5 mM/100 mM	60 °C
Mo(tfd-$COCF_3$)$_3$	CT-Solv.180	dispersion	R.T.
TPA-X	acetonitrile	1.5 mM	45 °C

Supplementary Table S1: **Summary of combinations of dopant, solvent, concentration of dopant, and process temperature used in this work.** Here, X in TPA-X represents a counter-anion: PF_6, $SbCl_6$, or TFSI.

1.2 Characterization of doping

UV-vis-NIR spectroscopy. Thin-film UV-vis-NIR spectra were acquired for thin films on glass substrates in air using a JASCO spectrometer (V-670).

PYS measurements. PYS data were obtained for thin films on ITO substrates with a SUMITOMO PYS-202 instrument.

XRD measurements. Out-of-plane and in-plane XRD data were acquired using a RIGAKU SmartLab with a MicroMax-007HF X-ray generator, employing Cu Kα radiation ($\lambda = 0.15418$ nm) in conjunction with a Si substrate with a naturally formed oxide layer or an EAGLE XG glass substrate.

We have detailed anomalous behavior in the (h00)-dependent XRD intensities for highly doped PBTTT in the main text, specifically for TPA-TFSI doped PBTTT. A similar trend was also obtained for another dopant, TPA-$SbCl_6$, (Fig. S1), where the (300) diffraction peak disappears, with its intensity comparable to the noise level of the XRD measurements.

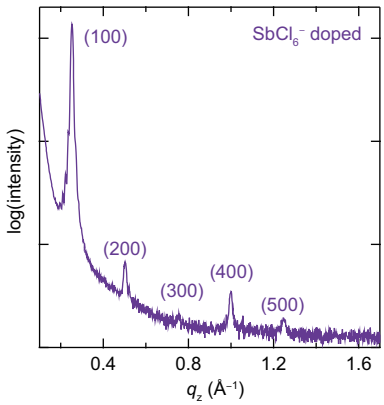

Supplementary Figure S1: **Out-of-plane XRD profile for TPA-$SbCl_6$ doped PBTTT.**

In an ideal single crystal, the full width at half maximum (FWHM) of a diffraction peak is independent of the diffraction order. On the other hand, it is known that the FWHM of diffraction peaks for paracrystalline materials, such as polymers, increases as the diffraction order increases,[3] and thus the degree of paracrystallinity can be estimated from an analysis of the FWHM. Figure S2 shows the FWHM of (h00) diffraction peaks for pristine and doped PBTTT thin films. It is found that the FWHM increases quadratically rather than linearly with the diffraction order, which is consistent with the model used for

paracrystalline materials.[4] Although the number of obtained diffraction orders may not be sufficient for precise analysis, the slope for TPA-$SbCl_6$ and TPA-TFSI doped PBTTT shows a remarkable reduction by a factor of 74% compared to that for pristine sample, and by a factor of 43% compared to that of F4TCNQ doped PBTTT, which demonstrates that the degree of paracrystallinity is effectively suppressed after doping with TPA-X.

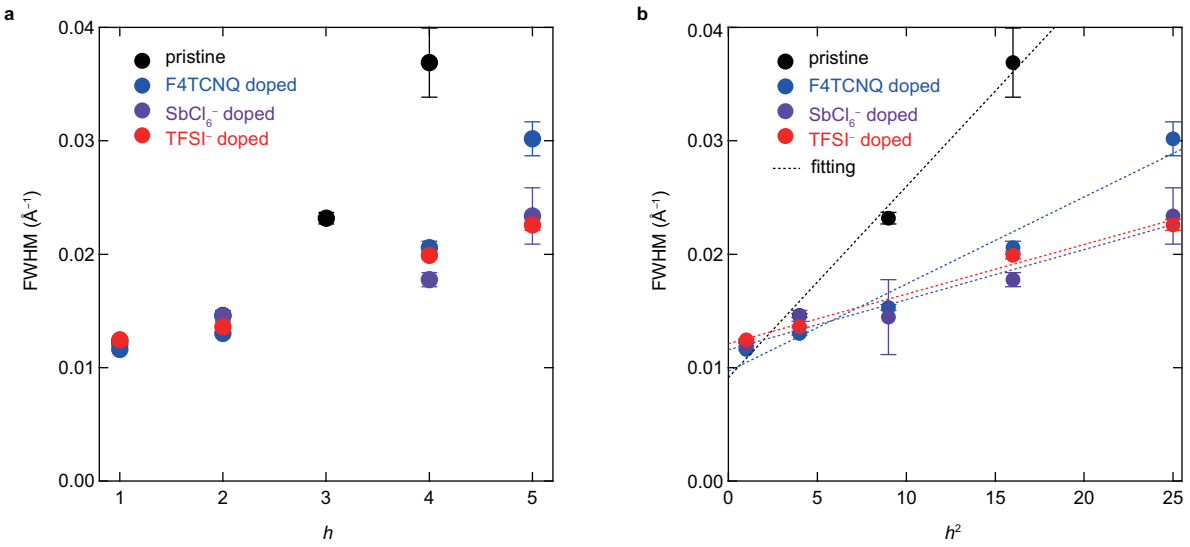

Supplementary Figure S2: **FWHM of diffraction peaks dependent on diffraction order.** FWHM values of (h00) diffraction peaks for pristine and doped PBTTT thin films. The data are plotted with a horizontal axis of **a**. h and **b**. square of h. The dashed plots show the results of linear fittings. The error bars for the FWHM were determined from the uncertainty in the fitting and represent one standard deviation.

1.3 Simulation of X-ray diffraction

A. Analysis of X-ray diffraction

In the main text, the intensities of the X-ray diffraction peaks, I_{h00}, were reproduced by electron density simulations along the z-axis (the out-of-plane direction of PBTTT thin films). I_{h00} for a given diffraction index ($h00$) is expressed as

$$I_{h00} = I_0 |F_{h00}|^2 P(\theta_{h00}) L(\theta_{h00}), \tag{1}$$

where F_{h00}, $P(\theta_{h00})$, $L(\theta_{h00})$, and θ_{h00} are the structure factor, polarization factor, Lorentz factor, and diffraction angle for a given ($h00$) diffraction, respectively.[5] $P(\theta_{h00})$ accounts for the angular dependence of Thomson scattering, which is described for electromagnetic dipole radiation as $P(\theta_{h00}) = (\sin^2\theta_{h00}\cos\theta_{h00})^{-1}$. $L(\theta_{h00})$ represents a geometrical factor determined by considering the real-space processes, and is unique for an individual measurement set up. In our simulation, the Lorentz parameter, $L(\theta_{h00}) = (1+\cos^2\theta_{h00})/2$, which is typically used for a single-crystal sample, was employed because the structural periodicity along the out-of-direction of PBTTT thin films should be good enough to be treated as a single crystal. The structural factor F_{h00} is defined by the following equation employing an electron density $n(x, y, z)$:

$$F_{hkl} = \iiint_{\text{unit cell}} n(x,y,z) \exp\left[2\pi i \left(\frac{hz}{d_{h00}} + \frac{kx}{d_{0k0}} + \frac{ly}{d_{00l}}\right)\right] dx\, dy\, dz. \tag{2}$$

For diffractions along the out-of-plane direction, k and l in the above equation are zero:

$$F_{h00} = \iiint_{\text{unit cell}} n(x,y,z) \exp\left(2\pi i \frac{hz}{d_{h00}}\right) dx\, dy\, dz \tag{3}$$

$$= \int_0^{d_{h00}} N(z) \exp\left(2\pi i \frac{hz}{d_{h00}}\right) dz, \tag{4}$$

where d_{h00} is the d-spacing and $N(z)$ is a one-dimensional electron density profile along the z-axis (electron densities across the xy plane are projected on the z-axis), defined as

$$N(z) = \int_0^{d_{00l}} \int_0^{d_{0k0}} n(x,y,z)\, dx\, dy. \tag{5}$$

In our simulation, density functional theory (DFT) calculations using Gaussian 09 were initially employed to obtain electron densities for each component of pristine and doped

PBTTT thin films; electron densities for a monomer of PBTTT backbone without alkyl chains, an alkyl chain (all-trans conformation), and anions were separately calculated. The B3LYP functional and the 6-31+G(d) basis set were employed, except for the Sb atom, for which the Lanl2DZ basis set was employed. These electron densities were projected into the z-axis to give one-dimensional electron density profiles along the out-of-plane direction. This electron density profile of a monomer unit was then employed to produce the profile of a z-axis periodic PBTTT lattice with the experimentally determined d_{100}, as shown in Fig. 3 in the main text. We introduce four variable parameters: z_{anion}, the weighted-center position of an anion relative to that of the polymer, ϕ_{alkyl}, the tilting angle of alkyl chains relative to the out-of-plane direction, n_{anion}, the number of anions per monomer of PBTTT, and σ, the degree of Gaussian disorder. These four variable parameters were optimized by the least squares method so that the simulated intensities of (h00) diffraction peaks match the experimental intensities. Considering the inversion symmetry of a PBTTT monomer, we assumed that anions reside symmetrically with a PBTTT monomer in the z-axis. To account for the finite structural disorder and molecular vibrations in thin films, $N(z)$ was then convoluted with the Gaussian distribution function $g(z;\sigma) = \exp(-z^2/(2\sigma^2))/\sqrt{2\pi\sigma^2}$ to obtain a blurred electron density profile N'(z):

$$N'(z) = N(z)g(z;\sigma). \tag{6}$$

Note that this treatment is equivalent to multiplying the Debye–Waller factor by the calculated peak intensity after a Fourier transformation. The convolution with the Gaussian distribution function acts as a low-pass filter in reciprocal lattice space and diminishes the peak intensities for higher-order diffraction. For an accurate evaluation of the crystallinity through peak shape analysis, molecular vibrations and static disorders, such as defects, should be taken into account. However, our focus here is to examine the structures of doped films and to interpret the origin of the disappearance of the (300) diffraction peak. Thereby, both types of disorders were treated jointly as a simple Gaussian disorder.

Simulation for pristine PBTTT. With an experimentally determined d_{h00} of 21.4 Å for a pristine PBTTT thin film, and the reported angle of alkyl chains ϕ_{alkyl} of 27°,[2] the variable parameter, the degree of disorder σ, was fitted so that the (h00)-dependent diffraction intensities are reproduced. As a result, a monotonic decay of diffraction intensities with

respect to the Miller index was well reproduced with $\sigma = 2.2 \pm 0.3$ Å, as shown in Fig. 3d in the main text.

Simulation for doped PBTTT. In the simulation for doped PBTTT thin films, anions, *e.g.*, $TFSI^-$ and $SbCl_6^-$, were introduced in the above simulation. The conformation of the anions relative to the PBTTT backbone was simulated by DFT calculations as follows: an initial conformation of the anions was evaluated for an isolated state by DFT calculations, then the pre-determined conformation was used to determine the relative conformation such that the resulting PBTTT-anion forms energetically favorable ion-pairs. For an isolated state of a TFSI anion, it was found that a *trans* conformation is energetically favorable compared to a *cis* conformation. During XRD simulation, the relative conformation was fixed, as shown in Fig. 3 in the main text. These conformations are likely to be more reasonable than those obtained in previous studies.[6] Note that the ambiguity in the conformation of anions relative to the polymer backbone does not affect the simulation results because the introduced structural disorder, σ, for the present system is relatively large and the resulting, blurred electron density of anions allows spatial smoothing.

Fitting of the (h00) diffraction peak intensities was conducted by the of least squares method with four variable parameters, z_{anion}, n_{anion}, ϕ_{alkyl}, and σ. Note that the fitting was done so that the common logarithm of the simulated (h00) peak intensities matched that of the experimental intensities. To ensure that the global minimum is achieved during the fitting, the global optimization algorithms Adaptive Memory Programming for Global Optimization (AMPGO)[7] and Basin-hopping[8] were employed, which use various initial states and a random seed.

We set proper binding conditions for four variable parameters to avoid an unrealistic conformation and short contact between the polymer backbone and anion (Table S2).

Supplementary Table S2: **Binding conditions for variable parameters.**

parameter	binding condition
ϕ_{alkyl}	10–40°
z_{anion}	0–$d_{h00}/2$ Å
n_{anion}	0–1.5
σ	0–$d_{h00}/10$ Å

B. Origin of disappearance of (300) diffraction peak

Our simulation based on the reconstruction of the electron density reproduced the experimentally obtained disappearance of the (300) diffraction peak for PBTTT doped with TPA-TFSI. Here, we qualitatively discuss how the destructive interference of scattered X-rays occurs. Given that the inversion symmetry for the PBTTT-TFSI system is maintained, its electron density profile can be an even function. Then, the Fourier series that appears in Eq. (4) collapses to (Fourier cosine series expansion)

$$F_{h00} = \int_0^{d_{h00}} N(z) \cos\left(2\pi \frac{hz}{d_{h00}}\right) dz. \tag{7}$$

We define $f_{h00}(z)$ as

$$f_{h00}(z) = N(z) \cos\left(2\pi \frac{hz}{d_{h00}}\right). \tag{8}$$

$N(z)$ and $f_{300}(z)$ are plotted in Fig. S3b. It is found that the z-position of the electron density reconstructed for a TFSI anion coincides with the first and third negative maxima of the cosine curve. This gives a large negative contribution to $f_{300}(z)$. Thus, F_{300} becomes zero; destructive interference of X-rays scattered by the PBTTT backbones and TFSI anions occurs for the (300) diffraction.

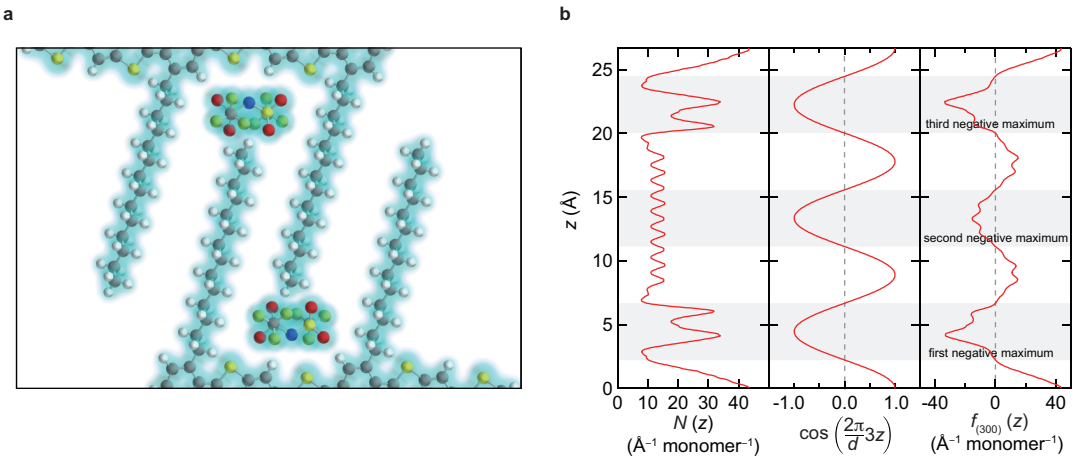

Supplementary Figure S3: **Analysis of electron density profile. a**. Illustration of TFSI doped PBTTT. **b**. Left panel: Electron density profile, $N(z)$, of TPA-TFSI doped PBTTT. Middle panel: Cosine curve in Eq. (8). Right panel: $f_{300}(z)$.

C. Reliability of simulation

Although we show the global minimum obtained in the fittings, it is possible that local minima exist. To clarify this, fittings of diffraction peak intensities were conducted while varying the position of anions z_{anion}. The other variable parameters, ϕ_{alkyl}, n_{anion} and σ, were optimized at a given z_{anion} with the algorithm AMPGO. In Fig. S4, ratios of simulated peak intensities $I_{h00,\,\mathrm{sim}}$ to experimental intensities $I_{h00,\,\mathrm{exp}}$ are plotted for each Miller index as a function of the position of the TFSI anion z_{anion}. Here, when $I_{h00,\,\mathrm{sim}}/I_{h00,\,\mathrm{exp}} = 1$ (illustrated as a shaded area along the horizontal axis), the local minimum of the simulation at that Miller index is obtained. On the other hand, the global minimum of the simulation is found at a limited z_{anion} where $I_{h00,\,\mathrm{sim}}/I_{h00,\,\mathrm{exp}} = 1$ for all Miller indexes. As a result, we obtained $z_{\mathrm{anion}} = 5.0$–5.1 Å as the global minimum. The sum of the squared residuals, χ^2, defined as

$$\chi^2 = \sum_{h=2}^{5} \left(\log I_{h00,\mathrm{sim}} - \log I_{h00,\mathrm{exp}}\right)^2, \tag{9}$$

shows that the present simulation can find the global minimum, as shown in Fig. S4.

Similarly, the global minimum of the fitting for PBTTT-$SbCl_6$ was found in a narrow band of z_{anion} (Fig. S5). Two possible minima were found at smaller $z_{\mathrm{anion}} \sim 4.0$–$4.2$ Å and larger $z_{\mathrm{anion}} \sim 4.4$–$5.1$ Å. It is concluded that a higher z_{anion} minimum is plausible, whereas a lower z_{anion} minimum gives an apparent short contact between the polymer backbone and the $SbCl_6$ anion.

The reliability of our simulation was assessed with varying amount of dopants n_{anion}. Fitting was conducted, optimizing the three variable parameters ϕ_{alkyl}, z_{anion}, and σ for a given n_{anion} with the algorithm AMPGO. In Figs. S6 and S7, ratios of the simulated peak intensities $I_{h00,\,\mathrm{sim}}$ to experimental intensities $I_{h00,\,\mathrm{exp}}$ are plotted for each Miller index as a function of n_{anion}. The global minimum of the simulation was found with $n_{\mathrm{anion}} = 0.91 \pm 0.03$ for TFSI and 1.09 ± 0.15 for $SbCl_6$. These results are consistent with the half-filled state derived from the Hall effect measurements. It was verified that although a relatively large error is found for ϕ_{alkyl}, this does not decrease the reliability of our simulation because changes in ϕ_{alkyl} are found to be less sensitive to modulations in XRD intensities.

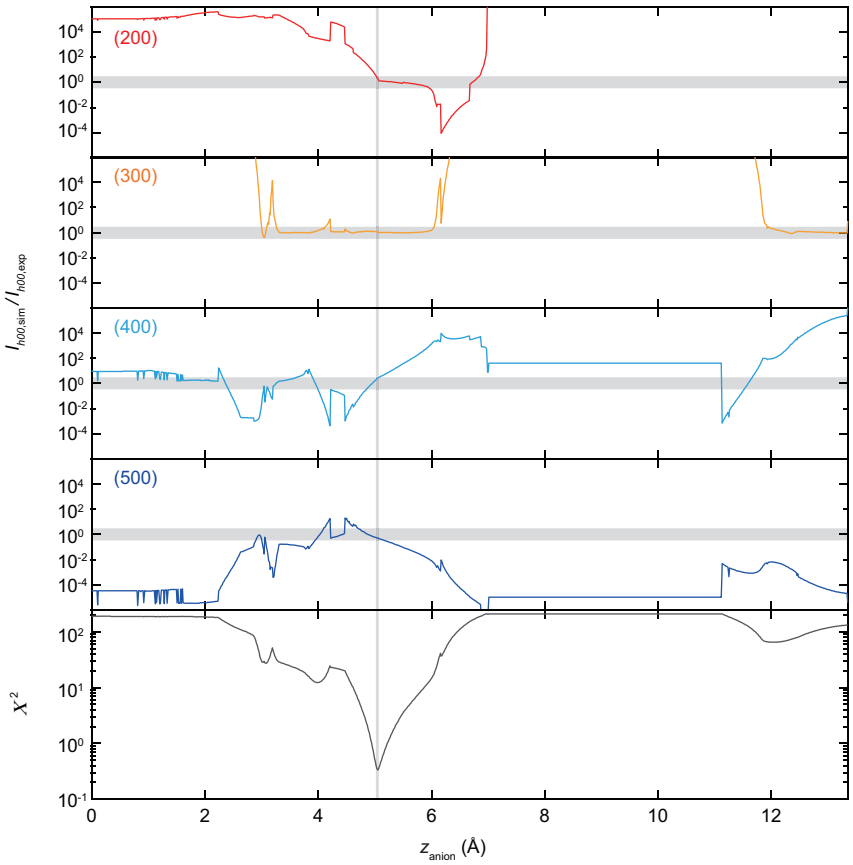

Supplementary Figure S4: **Estimation of TFSI anion position.** Ratios of simulated peak intensities $I_{h00,\,\mathrm{sim}}$ to experimental intensities $I_{h00,\,\mathrm{exp}}$ plotted for each Miller index as a function of the position of the TFSI anion z_{anion}. The sum of the squared residuals, χ^2, is also plotted. When $I_{h00,\,\mathrm{sim}}/I_{h00,\,\mathrm{exp}} = 1$ (illustrated as a shaded area along the horizontal axis), the local minimum of the simulation at that Miller index is obtained.

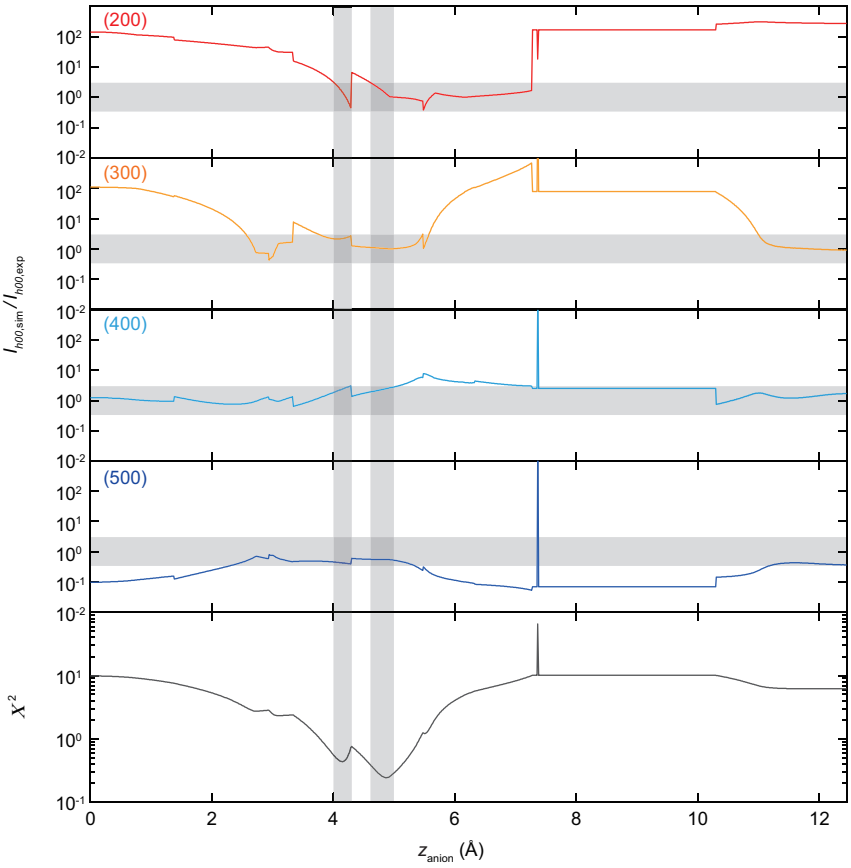

Supplementary Figure S5: **Estimation of $SbCl_6$ anion position.** Ratios of simulated peak intensities $I_{h00,\,\mathrm{sim}}$ to experimental intensities $I_{h00,\,\mathrm{exp}}$ plotted for each Miller index as a function of the position of the $SbCl_6$ anion z_{anion}. The sum of the squared residuals, χ^2, is also plotted. When $I_{h00,\,\mathrm{sim}}/I_{h00,\,\mathrm{exp}} = 1$ (illustrated as a shaded area along the horizontal axis), the local minimum of the simulation for that Miller index is obtained.

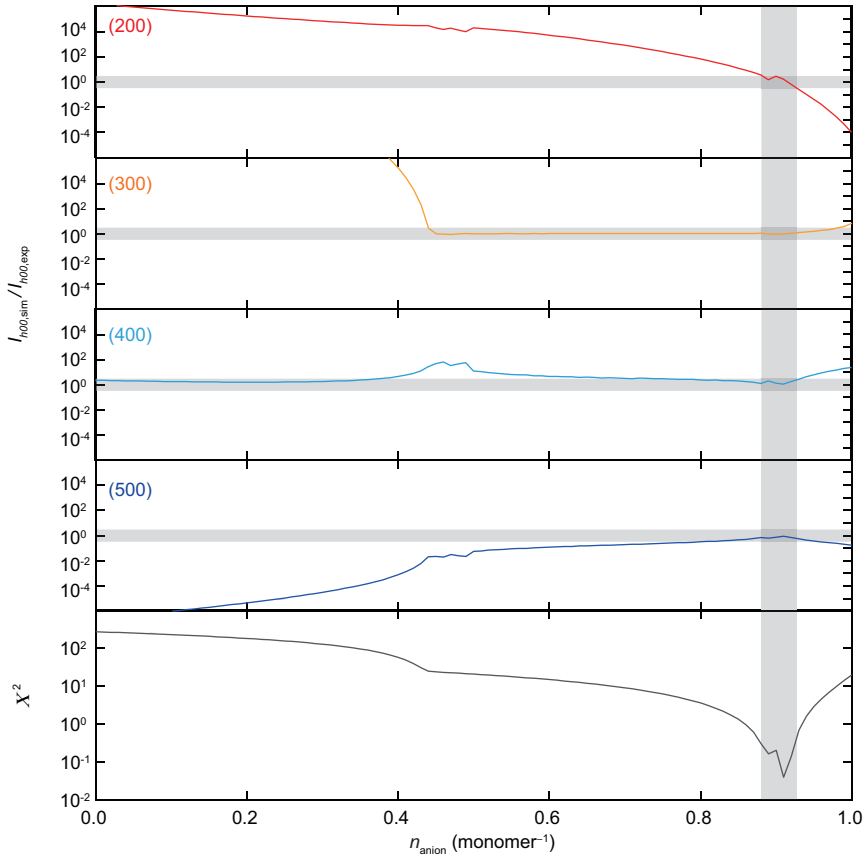

Supplementary Figure S6: **Estimation of doping level with TFSI anion.** Ratios of simulated peak intensities $I_{h00,\,\mathrm{sim}}$ to experimental intensities $I_{h00,\,\mathrm{exp}}$ plotted for each Miller index as a function of n_{anion}. The sum of the squared residuals, χ^2, is also plotted. When $I_{h00,\,\mathrm{sim}}/I_{h00,\,\mathrm{exp}} = 1$ (illustrated as a shaded area along the horizontal axis), the local minimum of the simulation for that Miller index is obtained.

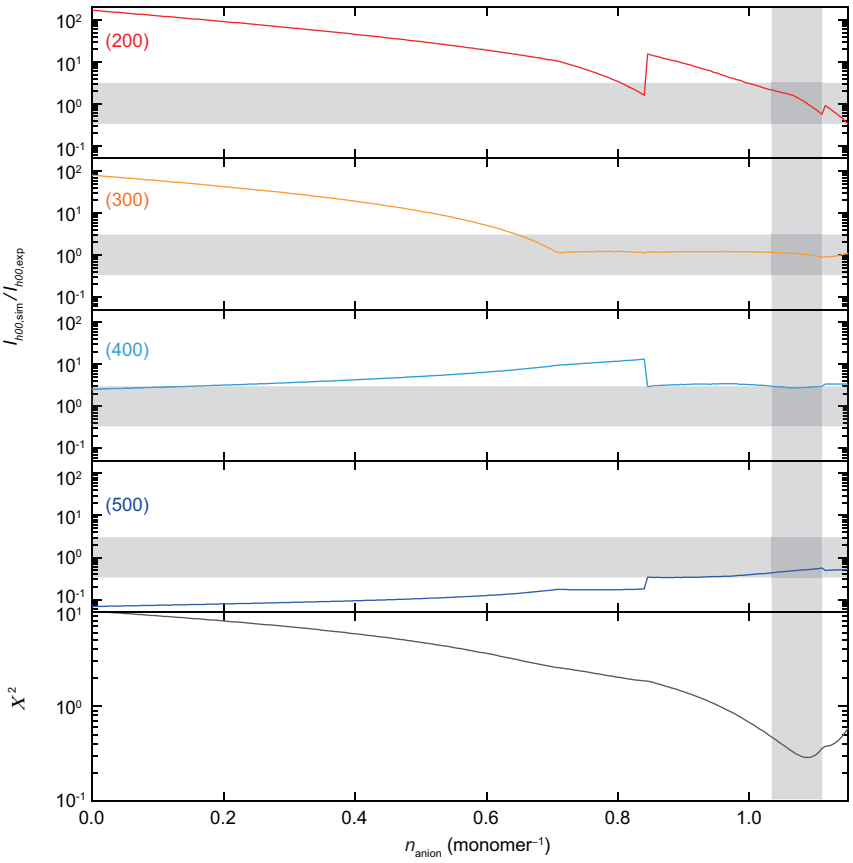

Supplementary Figure S7: **Estimation of doping level with $SbCl_6$ anion.** Ratios of simulated peak intensities $I_{h00,\,\mathrm{sim}}$ to experimental intensities $I_{h00,\,\mathrm{exp}}$ plotted for each Miller index as a function of n_{anion}. The sum of the squared residuals, χ^2, is also plotted. When $I_{h00,\,\mathrm{sim}}/I_{h00,\,\mathrm{exp}} = 1$ (illustrated as a shaded area along the horizontal axis), the local minimum of the simulation for that Miller index is obtained.

1.4 Analysis of X-ray photoelectron spectroscopy

X-ray photoelectron spectroscopy (XPS) was employed to evaluate the atomic composition of the doped PBTTT films, to further verify the half-filled state observed in the XRD analysis. XPS was performed using KRATOS ULTRA 2 with monochromatic Al Kα X-rays. We focused on the C 1s and F 1s spectra for TPA-TFSI doped PBTTT thin film to determine the ratio of fluorine to carbon atoms. The theoretical atomic composition of materials employed in our experiments are shown in Table S3. Note that it is assumed that the $TPA^{\bullet+}$ is absent in the thin film.

Supplementary Table S3: **Atomic composition of each molecule for the employed materials.**

material	carbon	nitrogen	oxygen	fluorine	sulfur	bromine
PBTTT	52	0	0	0	4	0
$TFSI^{-}$	2	1	4	6	2	0
$TPA^{\bullet+}$	18	1	0	0	0	3

Figure S8a shows the XPS survey scan for TPA-TFSI doped PBTTT thin film prepared in the same manner as in the XRD experiments. In the survey scan, all the atoms in Table S3 were observed. High-resolution spectra were obtained in narrow energy ranges to determine the composition of carbon (Fig. S8b) and fluorine (Fig. S8b) atoms, while changing the angle of the substrate θ_{sub}, defined as the angle between the surface normal and photoelectron trajectory.

XPS is a surface sensitive measurement owing to the short mean free path of a photoelectron (λ), typically a few nanometers in a solid film. The probability for a photoelectron to escape a solid film decreases exponentially with the depth from the surface, z_{sur}. When the substrate is tilted, the effective distance required for the photoelectron to travel in the solid film increases, which makes the measurement more sensitive to the surface. The probability, ϕ_{es}, for a photoelectron to escape from a position z_{sur} follows the relationship[9]

$$\phi_{\mathrm{es}} \propto \exp\left(-z_{\mathrm{sur}}/\lambda \cos\theta_{\mathrm{sub}}\right). \tag{10}$$

The normalized ϕ_{es} is plotted in Figs. S9a and b, where the mean free path of a photoelectron $\lambda = 3$ nm was used.[10] The depth at which ϕ_{es} is reduced to $1/e$ was estimated to be 3 nm for

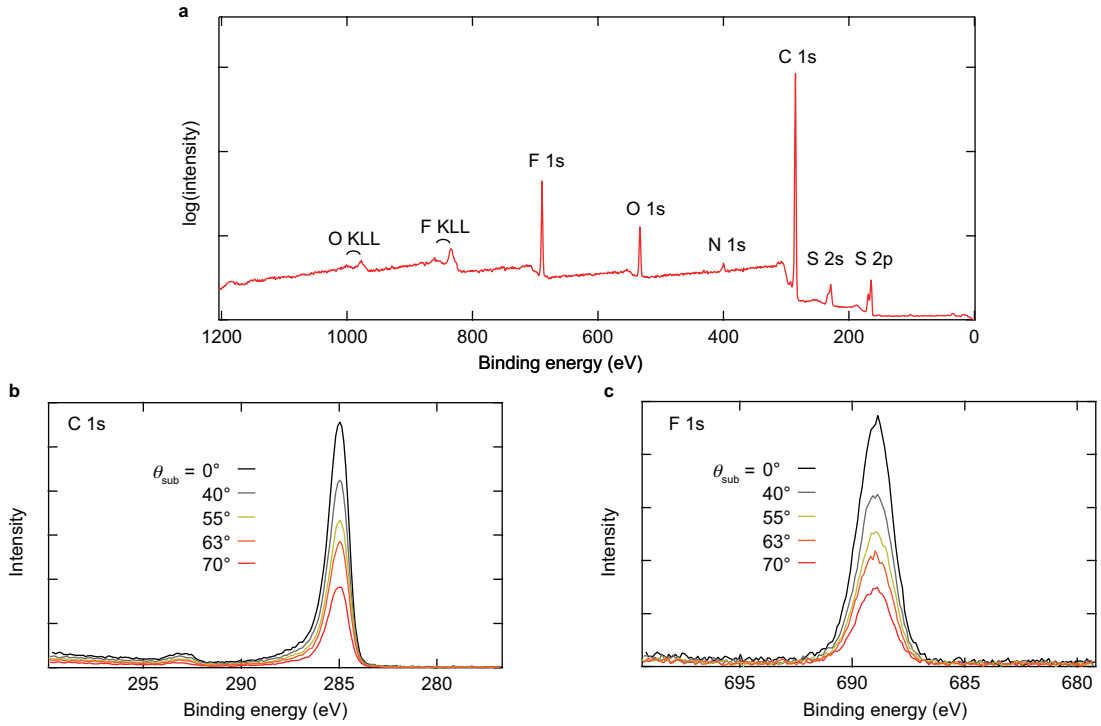

Supplementary Figure S8: **XPS spectra obtained for TFSI$^-$doped PBTTT thin film.** **a**. XPS survey scan for TPA-TFSI doped PBTTT thin film. Narrow spectra for **b**. C 1s and **c**. F 1s for various substrate tilting angles θ_{sub}.

$\theta_{\mathrm{sub}} = 0°$, and becomes about 1 nm for $\theta_{\mathrm{sub}} = 70°$. This means that the first molecular layer dominates the XPS spectrum for $\theta_{\mathrm{sub}} = 70°$, whereas a few molecular layers from the surface contribute to the spectrum for $\theta_{\mathrm{sub}} = 0°$. Given the d-spacing in the out-of-plane direction was determined to be 2.67 nm, we can assume that the atomic composition in the bulk can be obtained with the latter condition. The atomic composition ratio (F/C) is calculated to be 0.117 at $\theta_{\mathrm{sub}} = 0°$and 0.111 at 70° (Fig. S9c). Because a depth insensitive F/C ratio was observed, it is evident that the present TPA-TFSI doping allows bulk doping with no excess of dopants on the surface. The F/C ratio experimentally obtained from XPS measurements (~ 0.117) is equivalent to the amount of TFSI anions $n_{\mathrm{anion}} = 0.86$ monomer^{-1}, which is in a perfect agreement with the result obtained from the XRD simulation.

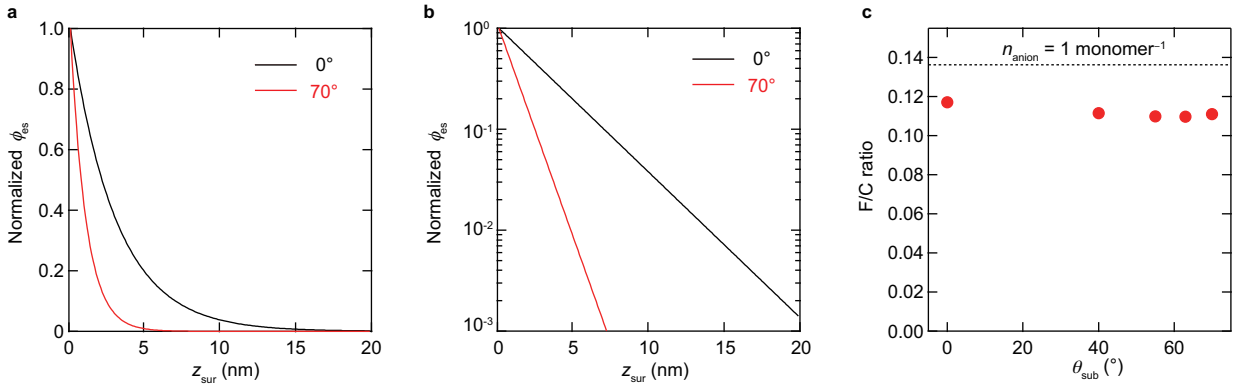

Supplementary Figure S9: **Depth dependence of photoelectron escape probability.** Normalized photoelectron escape probability ϕ_{es} as a function of z_{sur} on **a**. linear and **b**. logarithmic scales with substrate tilting angles of 0°and 70°. The mean free path λ was set to 3 nm. **c**. Evaluated angular dependence of F/C ratio of TPA-TFSI doped PBTTT thin film. The F/C ratio for an ideal half-filled state, 0.133, is shown as a black dotted line.

1.5 Device fabrication and transport measurements

Device fabrication. Hall effect measurements were performed using a Hall bar geometry, where the doped PBTTT thin film was patterned by dry etching in order to perform precise measurements of local potentials of probes along a channel. The Hall bar devices were fabricated on a 0.7-mm-thick EAGLE XG glass substrate pre-cleaned by sonication in acetone and isopropanol. Cr (3 nm) and Au (30 nm) electrodes were thermally evaporated in conjunction with a standard double layer lift-off process to form a channel length L and width W of 320 μm and 80 μm, respectively. After evaporation of the electrodes, the devices were further cleaned with acetone and isopropanol. The PBTTT thin film was deposited in a similar manner and then patterned into the Hall bar geometry by laser etching using an yttrium aluminum garnet (YAG) laser. After the doping process, each device was encapsulated with CYTOP 809M (AGC Chemicals). A photographic image of the Hall bar used in this work is shown in Fig. S10.

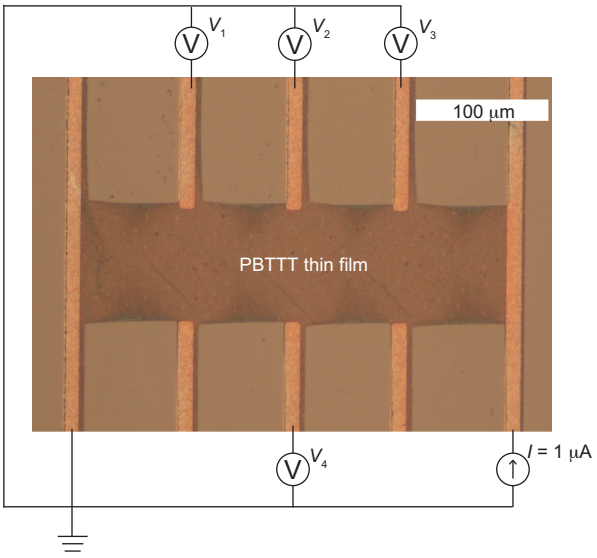

Supplementary Figure S10: **Photographic image of the Hall bar used in this work.** Optical microscopy image of the Hall bar used for magnetotransport measurements. A PBTTT thin film was patterned into the Hall bar geometry by laser etching, applying a channel length, L, and channel width, W, of 320 and 80 μm, respectively. Four-point-probe conductivity values and Hall coefficients were determined using longitudinal voltage probes V_1, V_2, and V_3 and transverse probes V_2–V_4.

Hall effect measurements. Hall effect measurements were performed using a He gas

exchanged cryostat with a superconducting magnet (Mercury System, Oxford Instruments) along with a KEITHLEY 2400 source meter and KEYSIGHT 34465A 6 1/2 digital multimeter. Both the longitudinal and transverse electromotive forces were monitored simultaneously while applying a dc current of 1 μA and sweeping the magnetic field from 10 T to -10 T at a rate of approximately 0.2 T min^{-1}.

1.6 Fabrication and doping of thick films

All the fabrication and doping processes were conducted in an Argon purged glove box. A thick (5 μm) PBTTT film was fabricated by a modified push-coating method.[11] A droplet of 3-wt% PBTTT solution was placed on an elastomer sheet composed of a tri-layer of polydimethylsiloxane (PDMS)/fluorinated polymer (SIFEL®, Shin-Etsu Chemical Co. Ltd.)/PDMS at room temperature. The droplet was then covered with an EAGLE XG glass for 2 hours. Solvent evaporation that may take place through the PDMS substrate prevents the "coffee ring" effect, and gives a homogeneous thick polymer film. The PBTTT thick film deposited on the glass substrate was then peeled off from the PDMS substrate. Thick films were annealed at 180 °C for 2 hours on a hot plate.

A 5-μm-thick PBTTT film was doped in a similar manner as for the thin films. The thick films were immersed into a TPA-TFSI solution at 45 °C for 2 hours. During this doping process, the TPA-TFSI solution was replaced with a fresh solution. Doped films were then dried on a hot plate at 80 °C for 1 hour to evaporate solvent inside the film prior to XRD measurements. Note that further optimization of the process may improve doping efficiency.

1.7 Conformation of anions

To speculate the conformation of anions relative to PBTTT backbone, we initially constructed two-dimensional PBTTT cation structure (3 chains) based on the crystallographic data, where the structure of each cation monomer unit was optimized by DFT calculation. This determined the initial void that is composed of alkyl side chains of PBTTT. Because our XRD analysis concluded that the weight-center position of TFSI is 5.1 Å away from that of PBTTT backbone, the initial position of TFSI is considered to be limited. Starting from this initial position, the conformation of TFSI was further optimized. Although that the obtained conformation might not find a global minimum in energy during the structural optimization, it is reasonable to say that the obtained conformation of TFSI is realistic enough because 5.1 Å distance is found to be reproduced after the optimization. The conformation of TFSI has a finite degree of freedom, in particular, rotational degree of freedom along the molecular long axis of TFSI. However, this does not impact on the degree of void filling; in any situation, the nitrogen and two of the four oxygen sites in the TFSI anions that should interact strongly with the H_2O molecules are sterically protected by the polymer backbone, and become inaccessible to H_2O molecules. Raman and infrared spectroscopies in conjunction with DFT calculations will be helpful to identify the conformation of TFSI relative to the polymer backbone, which will be addressed in future.

2. Supplementary references

[1] McCulloch, I. *et al.* Liquid-crystalline semiconducting polymers with high charge-carrier mobility. *Nature Materials* **5**, 328 (2006).

[2] Cho, E. *et al.* Three-dimensional packing structure and electronic properties of biaxially oriented poly(2,5-bis(3-alkylthiophene-2-yl)thieno[3,2-*b*]thiophene) films. *Journal of the American Chemical Society* **134**, 6177–6190 (2012).

[3] Rivnay, J., Noriega, R., Kline, R. J., Salleo, A. & Toney, M. F. Quantitative analysis of lattice disorder and crystallite size in organic semiconductor thin films. *Physical Review B* **84**, 045203 (2011).

[4] Factor, B. J., Russell, T. P. & Toney, M. F. Grazing incidence X-ray scattering studies of thin films of an aromatic polyimide. *Macromolecules* **26**, 2847–2859 (1993).

[5] Warren, B. E. *X-ray Diffraction* (Courier Corporation, 1990).

[6] Yamashita, Y. *et al.* Efficient molecular doping of polymeric semiconductors driven by anion exchange. *Nature* **572**, 634–638 (2019).

[7] Lasdon, L., Duarte, A., Glover, F., Laguna, M. & Martí, R. Adaptive memory programming for constrained global optimization. *Computers & Operations Research* **37**, 1500–1509 (2010).

[8] Wales, D. J. & Doye, J. P. Global optimization by basin-hopping and the lowest energy structures of Lennard-Jones clusters containing up to 110 atoms. *The Journal of Physical Chemistry A* **101**, 5111–5116 (1997).

[9] Cumpson, P. J. Angle-resolved XPS and AES: depth-resolution limits and a general comparison of properties of depth-profile reconstruction methods. *Journal of Electron Spectroscopy and Related Phenomena* **73**, 25–52 (1995).

[10] Tanuma, S., Powell, C. J. & Penn, D. R. Calculations of electron inelastic mean free paths. V. Data for 14 organic compounds over the 50–2000 ev range. *Surface and Interface Analysis* **21**, 165–176 (1994).

[11] Ikawa, M. *et al.* Simple push coating of polymer thin-film transistors. *Nature Communications* **3**, 1176 (2012).